

Velocity map imaging as a tool for gaining mechanistic insight from closed-loop control studies of molecular fragmentation

Bethany Jochim,¹ R. Averin,¹ Neal Gregerson,¹ J. McKenna,² S. De,² D. Ray,² M. Zohrabi,² B. Bergues,³ K. D. Carnes,² M. F. Kling,^{2,3} I. Ben-Itzhak,² and E. Wells^{1,*}

¹*Department of Physics, Augustana College, Sioux Falls, South Dakota 57197, USA*

²*J. R. Macdonald Laboratory, Department of Physics, Kansas State University, Manhattan, Kansas 66506, USA*

³*Max Planck Institute of Quantum Optics, Hans-Kopfermann Strasse 1, D-85748 Garching, Germany*

(Received 21 December 2010; published 27 April 2011)

Strong-field closed-loop control schemes using shaped ultrafast laser pulses have been used to selectively fragment a variety of molecules in recent years. The resulting pulses are often complex and resist an easy mechanistic interpretation. We report on the use of velocity map imaging to study the dissociative ionization of CO molecules by optimally-shaped ultrafast laser pulses. Using this technique, a mechanism is identified for the optimized $\text{CO}^+ \rightarrow \text{C} + \text{O}^+$ dissociation, and some of the observed control over the CO^+ dissociation branching ratio is ascribed to an angular discrimination effect. Furthermore, we demonstrate that the acquisition of two-dimensional velocity map images is rapid enough to incorporate directly into the adaptive control loop.

DOI: [10.1103/PhysRevA.83.043417](https://doi.org/10.1103/PhysRevA.83.043417)

PACS number(s): 32.80.Qk, 33.80.Rv, 42.50.Hz, 34.50.Gb

I. INTRODUCTION

There are now a number of examples of strong-field closed-loop schemes that control molecular fragmentation [1–18] by using ultrafast laser-pulse shaping [19] in conjunction with adaptive learning algorithms [20–22]. While there are many different methods for using intense ultrafast laser pulses to manipulate molecular dynamics (e.g., Refs. [23–26]), if general applicability is desired, the closed-loop scheme is among the most promising because it sidesteps the often complex problem of understanding the nonlinear response of the molecule in the strong laser field. Letting the molecule “solve its own Schrödinger equation,” as it is sometimes described, has some powerful advantages. Optimal control theory demonstrates that if the experiment does not suffer from excessive constraints, these adaptive search strategies should always find an optimal solution to a particular control problem [27]. As outlined in the review by Chakrabarti and Rabitz [28], it is often “surprisingly” easy to guide a system to reach a particular outcome using this adaptive femtosecond control.

On the other hand, the solutions generated are often complex and resist an easy mechanistic explanation. Reports of success at “reverse engineering” the optimal laser pulse and thereby recovering information about the dynamics involved in the interaction are relatively scarce [4,29–32]. These mechanistic questions are important because there is, so far, no general prescription for choosing relevant search parameters around which to structure the pulse characteristics. Poor choices of pulse parameters can lead to artificial traps in phase space, limiting the ability of the algorithm to find an optimal solution [33]. Moreover, working in the strong-field regime [5] can also complicate the control process [28]. Developing more robust strong-field control approaches will likely depend upon gaining a deeper understanding of the control mechanism(s).

Our approach to these mechanistic questions has centered on the role of the feedback signal. By making small, systematic changes to the target of the adaptive control, we hope to probe the dynamics of the molecular process that is being optimized. We have demonstrated that, at least for simple diatomic molecules, choosing a more specific feedback target (such as C^+ and O^+ that dissociate only from transient CO^+) results in correspondingly less complex optimal pulses [17]. We have also demonstrated that feedback may include a coincidence condition, allowing the direct targeting of a new group of states by the learning algorithm [18].

Velocity map imaging (VMI) [34,35] is a popular method of studying laser-molecule interactions, and recent work using this method includes an investigation of laser chirp-based control of molecular dissociation [36]. In this paper, we report on the use of VMI to recover mechanistic information about the selective dissociation of transient CO^+ ions following ionization by an intense ultrafast optimally-shaped laser pulse. The VMI method provides angle-resolved measurements of ion velocity which complement our previous measurements that relied on high-resolution time-of-flight spectrometry and were thus restricted to measuring the ion momentum along a single dimension.

While VMI cannot directly measure correlations between different particles from the same molecule like other momentum imaging methods, such as COLTRIMS [37], can, it has the advantage of a much shorter acquisition time. This is an attractive feature for closed-loop control experiments since the rapid data acquisition may allow VMI to be used directly as feedback [32,38,39]. If suitably incorporated into the learning loop, VMI offers the investigator the ability to select a very specific feedback target. Coupling this ability with various choices of control variables within the framework of adaptive control offers promise as a route to better understanding of these control methods. In Sec. III B, we report on the use of two-dimensional (2D) VMI as a source of feedback for closed-loop control. Drawing upon this experience using the raw 2D VMI as feedback, we discuss some of the experimental challenges of adopting image-based feedback and suggest some directions for future refinement.

*eric.wells@augie.edu

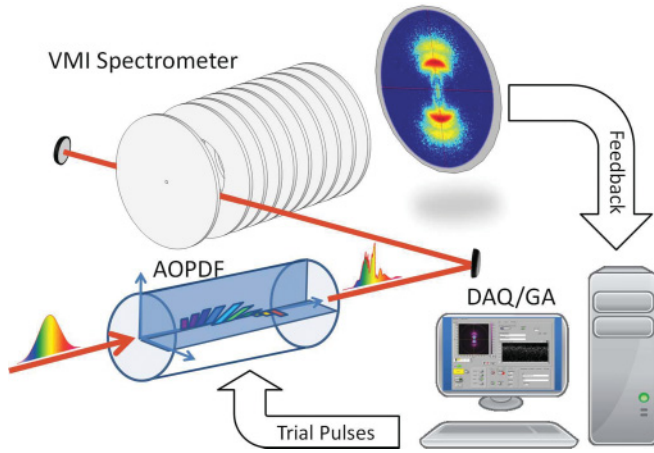


FIG. 1. (Color online) Conceptual picture of the experimental setup. The laser pulses from the Ti:sapphire oscillator are shaped by the AOPDF and then amplified and focused in the VMI spectrometer. An effusive jet directs the target gas into the spectrometer perpendicular to the laser beam. The 2D images are collected by the data acquisition system (DAQ) and either used for later analysis (as in Sec. III A) or, as depicted in the figure, used as feedback by the genetic algorithm (GA) as it searches for an optimal pulse. The latter variation of the experiment is described in Sec. III B.

II. EXPERIMENT

Our experimental setup consists of an ultrafast laser system with a pulse shaper, a VMI spectrometer, and a computer control that links them together and contains the genetic algorithm that uses the feedback signals to determine the optimal pulse shapes. A schematic of this configuration is shown in Fig. 1. The laser pulses are provided by a Ti:sapphire laser system with a multipass amplifier. The amplified pulses have a center wavelength of 790 nm, a pulse energy of up to 2 mJ, a repetition rate of up to 2 kHz, and a Fourier transform-limited (FTL) duration of 45 fs. Typical pulse energies in these experiments were 0.1 mJ, which corresponds to a peak intensity of approximately 10^{14} W cm $^{-2}$ after they are focused by an $f = 75$ mm spherical mirror. The pulse shaper is an acousto-optic programmable dispersive filter (AOPDF) [40].

The VMI spectrometer used in these experiments has been described in other publications [41,42]. As shown in Fig. 1, the laser passes through the spectrometer and is focused by the spherical mirror into an effusive jet target of CO molecules. Following ionization by the laser pulse, the ions were projected onto the microchannel plate-phosphor screen assembly and imaged by a CCD camera. As is standard with the VMI technique [34,35], the spectrometer ion optics ensure that all ions emerging from the laser focus with the same velocity vector strike the detector in the same location. The microchannel plates are fully powered only at times corresponding to the arrival of a single preselected ion species using a triggered high-voltage switch.

For the results described in Sec. III A, the pulse shaper was programmed to produce pulses that had previously been optimized using a time-of-flight measurement to maximize either $[C^+ + O]/[C + O^+]$ or $[C + O^+]/[C^+ + O]$ [17]. The pulse shapes were verified using a Second Harmonic Generation Frequency Resolved Optical Gating technique

[43]. We recorded multiple images of the C^+ and O^+ fragments with both the optimized and FTL pulses. The images were then inverted off-line to recover the three-dimensional (3D) velocity distribution from the raw 2D image. We employed three different inversion procedures [44–46] and compared the final results to verify that the outcomes were consistent. We used the inversion method described by Bordas and co-workers [44] for the results shown in this paper, although all three methods ultimately gave qualitatively similar results.

In Sec. III B, we demonstrate the use of the raw 2D VMI data to generate feedback for adaptive femtosecond control. The genetic algorithm used to search for optimal pulses is described in Ref. [17]. The integration time and microchannel plate voltage combination was selected so that the maximum intensity region of the image with a FTL pulse does not exceed the 12-bit capacity of the camera. In practice, this amounted to an integration of around 1000–1500 laser shots. For enhancing $[C^+ + O]/[C + O^+]$ or $[C + O^+]/[C^+ + O]$, two images (C^+ and O^+) are needed for each trial pulse. Thus, the total time for a single trial pulse was about 6 s, a duration that includes the time to acquire both images, adjust the delay of the high-voltage switch between ions, and load the trial pulse into the AOPDF. Fitness values were evaluated by integrating the image intensity within a preselected portion of the 2D image.

III. RESULTS AND DISCUSSION

Our initial goal in this experiment was to study the mechanism(s) leading to the dissociative ionization of CO following exposure to optimized laser pulses using velocity map imaging. The initial optimization used time-of-flight feedback and is described in Ref. [17]. Our studies of the dissociation using VMI are discussed in Sec. III A. In that section, we show that VMI measurements can produce information that allows the identification of plausible control pathways.

The next step in the experiment, described in Sec. III B, involves the use of VMI directly in the adaptive control loop. We were able to successfully use raw (2D) images as feedback for adaptive control. As with many nascent methods, however, a number of issues must be overcome before the technique is widely applicable. In this part of the paper, we focus on three questions: (1) What are the requirements for robust image-based feedback? (2) Could we use 2D VMI to obtain optimal pulses that were similar to the pulse obtained with time-of-flight feedback? (3) Is the raw 2D image sufficient for feedback purposes, or can it only be used in limited circumstances?

A. VMI studies of controlled dissociation

As we used previously identified laser pulses in this work, it is worth briefly reviewing the results of the earlier experiment [17]. In that work, the feedback signal was first selected to include all of the C^+ and O^+ ions produced in the interaction, which would include fragments originating from both CO^+ and CO^{q+} molecular ions. Using the resolution available from the time-of-flight spectrometer, the feedback gates were then adjusted to predominantly select fragments from the transient CO^+ ions. These narrow gates were used to optimize the $[C^+ + O]/[C + O^+]$ or $[C + O^+]/[C^+ + O]$ feedback targets. The optimal pulses produced fitness values either

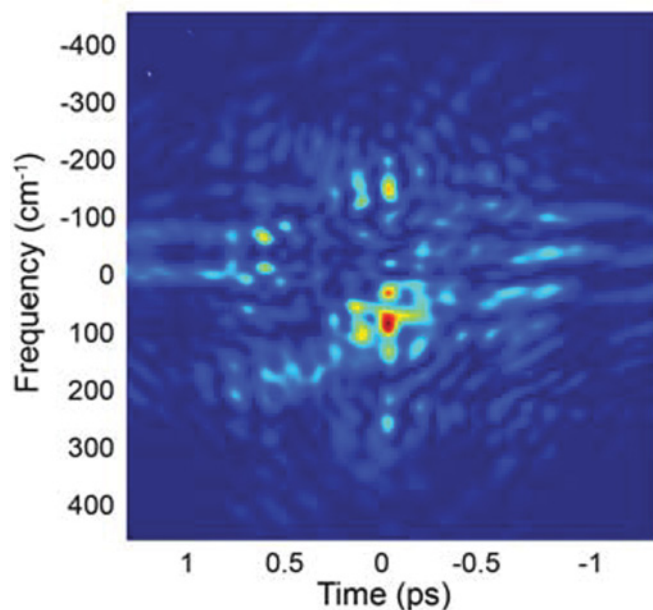


FIG. 2. (Color online) Polarization-gate frequency resolved optical gating (PG-FROG) representation, adapted from Ref. [17], of the shaped laser pulse that optimized $[C + O^+]/[C^+ + O]$. This pulse essentially doubled the $[C + O^+]/[C^+ + O]$ yield compared to a baseline FTL pulse. Section III A describes our examination of the underlying mechanisms.

essentially identical (for $[C^+ + O]/[C + O^+]$) or double (for $[C + O^+]/[C^+ + O]$) the value obtained with FTL pulses. Principal component analysis [47] of the optimal pulse

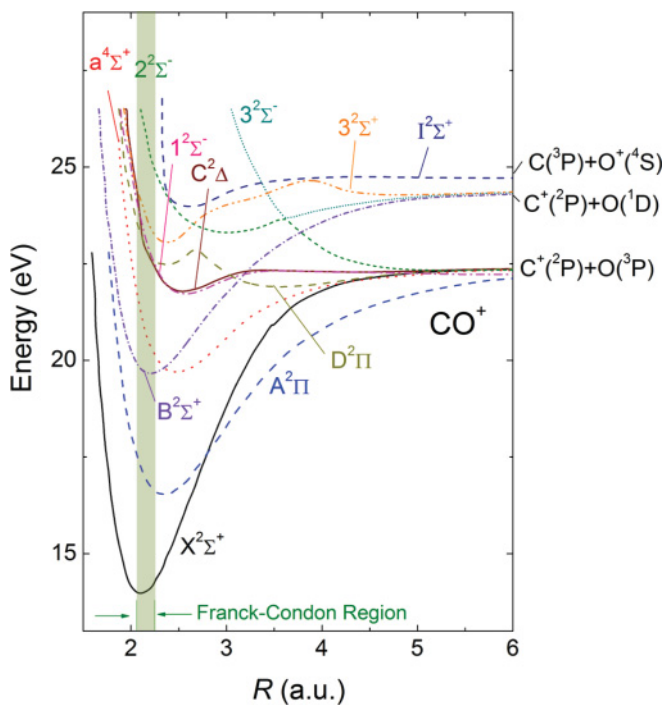


FIG. 3. (Color online) Potential energy curves for various states of CO^+ [48,49]. The lowest state that goes to $C + O^+$ at the separate atom limit is the $I^2\Sigma^+$ state. The shaded region represents the range of internuclear distances populated by Franck-Condon transitions from the CO ground state.

shapes showed that the pulses optimized with the more specific feedback could be expressed with fewer control directions and were thus in some sense simpler than the pulses obtained with feedback that included the entire ion species.

The most interesting of the previous pulses were the ones that optimized $[C + O^+]/[C^+ + O]$. Despite the fact that the lowest $C(^3P) + O(^4S)$ final state is more than 1 eV above the several states that go to $C^+(^2P) + O(^3P)$ in the dissociative limit, these pulses were less intense and had a complex structure, as shown in Fig. 2. In the time-of-flight experiment [17], the gain in the $[C + O^+]/[C^+ + O]$ fitness target was obtained by suppressing the C^+ channel compared to a FTL pulse while keeping the lowest-energy portion of the O^+ channel nearly at the same level. It is this result that we will examine in detail with VMI. The relevant potential-energy curves for CO^+ are shown in Fig. 3.

The optimal pulses were reproduced in this experiment, and the VMI images were obtained as explained above. After inversion we obtain a dissociation density plot as a function of the angle from the polarization axis (θ) and the kinetic-energy release (KER), as shown in Fig. 4. The images were also integrated over all angles to produce the KER spectrum shown in Fig. 5. Using this information, the ions produced from single ionization can be clearly identified as those below ~ 5 eV. This is established in conjunction with the fact that

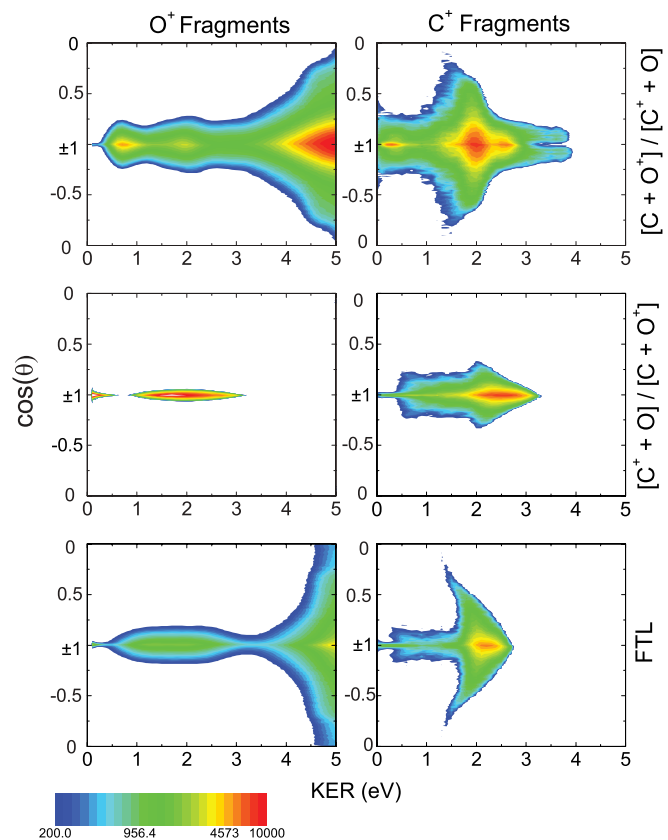


FIG. 4. (Color online) Density plot of dissociation as a function of KER and $\cos(\theta)$ for the $C + O^+$ (left) and $C^+ + O$ (right) channels for pulses tailored to optimize $[C + O^+]/[C^+ + O]$ (top) and $[C^+ + O]/[C + O^+]$ (middle) feedback targets, where θ is the angle between the laser polarization and the CO internuclear axis. The results obtained with a FTL pulse are shown on the bottom for comparison.

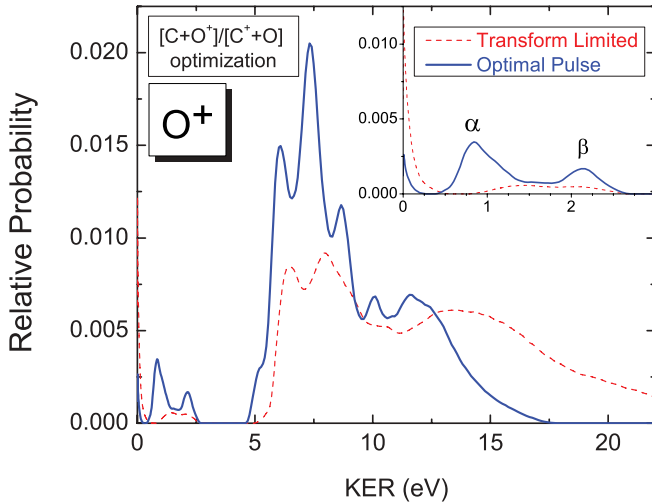


FIG. 5. (Color online) Relative probability vs KER for O^+ fragments produced by FTL pulses (dashed red line) and pulses that optimize $[C + O^+]/[C^+ + O]$ (solid blue line). The inset magnifies the single-ionization region below 3 eV.

the electron-impact ionization data of Lundqvist *et al.* [50] show that the lowest KER channels arising from CO^{2+} start above ~ 5 eV. Moreover, the observed angle-resolved KER distributions, shown in Fig. 4, depend on the selection of ion species. Above 5 eV, however, the O^+ and C^+ fragments yield similar distributions, suggesting this region is dominated by double ionization (i.e., $CO^{2+} \rightarrow C^+ + O^+$). For this reason, we are interested only in the portion of the image corresponding to KER less than 3 eV, displayed in the inset of Fig. 5.

While analysis of our results is hampered by a lack of CO^+ potential-energy curves that dissociate to $C + O^+$ at the separate atom limit, the results shown in Fig. 5 already allow us to draw several conclusions. If the dissociation is accomplished by population of the $I^2\Sigma^+$ state, which is the lowest state that dissociates into $C(^3P) + O(^4S)$ at the separate atom limit, then the shape of the $I^2\Sigma^+$ curve will influence the KER plot in Fig. 5. If the transition to the $I^2\Sigma^+$ state is nearly vertical, such as with a direct multiphoton ionization from the neutral molecule, or if a rescattered electron excites the molecule on its first return $\sim 2/3$ of a laser cycle after the initial ionization step, the most relevant part of the curve is strongly repulsive. Moreover, even though there is evidence [51] that later returns are important in the rescattering picture, the Franck-Condon overlap indicates that the lower vibrational levels of the $CO^+ X^2\Sigma^+$ state are predominantly populated, leaving little opportunity for the nuclear wave packet to extend to large R . With population limited, even for later recollision times, to the region around $R \approx 2.1\text{--}2.3$ a.u., these relatively fast mechanisms all lead to population that would be projected onto the strongly repulsive part of the $I^2\Sigma^+$ curve. While the calculated potential-energy curve [49] does not extend to a small enough internuclear distance to make a detailed calculation of the resulting KER distribution, a simple estimate based on a reflection method approach suggests that the KER distribution would be very wide (many eV) and extend down below 1 eV on the lower side. We do not see this sort of structure in Fig. 5.

In addition, it is worth noting that Znakovskaya *et al.* have shown that recollision excitation is a major process leading to dissociative ionization of CO for very short (4 fs) pulses [52]. While our 45 fs FTL pulses have enough intensity to give the recolliding electron up to 17 eV of energy, more than enough to reach the $I^2\Sigma^+$ state from the X or A electronic states of CO^+ , the optimal pulses shown in Fig. 2 [17] are much longer in duration, and therefore correspondingly less intense, since the phase-only pulse shaping approximately preserves the pulse energy. Projecting the optimal pulse structure shown in Fig. 2 onto the time axis and finding the full width at half maximum (FWHM) of the temporal profile, which is subsequently used to determine the peak intensity, we estimate the maximum recollision energy to be 3.2 eV. As a result, it is unlikely that the recollision mechanism can populate the high-lying states that dissociate to $C + O^+$.

The main features of the optimized $C + O^+$ dissociation channel KER, shown in the inset of Fig. 5, are two peaks, centered at 0.8 eV (labeled α) and 2.2 eV (β). Both of these peaks have FWHM of around 0.5 eV. Under the assumption that the process involves ionization followed by a subsequent dissociation, a Floquet model may be employed to determine the dissociation pathways leading to the observed KER distribution [53,54]. In the Floquet formulation, which uses diabatic field-dressed potential-energy curves, the absorption (emission) of n photons corresponds to the shifting of the potential-energy curve down (up) by $n\hbar\omega$. The dressed states are denoted by the state followed by $\pm n\omega$. The dissociating nuclear wave packet can make a transition at any crossing that obeys the molecular dipole selection rules. Pathway identification involves the systematic selection of dissociation routes and the elimination of those with properties inconsistent with the experimental results. While many pathways may contribute at small levels, we seek to explain the main features of the observed KER distribution using the simplest possible routes and the lowest number of photons.

A reasonable criticism of the Floquet approach is that the strong electric field of the laser can distort the potential-energy curves in ways not addressed by the model. This might be especially true when dealing with the complex pulse shapes studied here. An important point to remember, however, is that the observed KER distribution is dictated by the difference between the initial and final energy. Since the pathways begin to open at their low intensity threshold, it is unlikely that the initial curve crossings are distorted too much. The final energies (as $R \rightarrow \infty$) are likewise undisturbed, and so even though there may be considerable distortions of the path en route, the KER values will be relatively unaffected. For these reasons, this dressed state approach has previously been able to explain intense field experimental results rather well (e.g., Refs. [53–55]).

As a first step, we consider direct transitions from the $CO^+ X^2\Sigma^+$ ground state to the field-modified dissociative $I^2\Sigma^+$ state. A possible candidate path is $X^2\Sigma^+ \rightarrow I^2\Sigma^+ - 7\omega$, with a KER of 0.85 eV. The adjacent $X^2\Sigma^+ \rightarrow I^2\Sigma^+ - 8\omega$ path has a peak KER of 2.42 eV, which although slightly higher than our observations is probably still consistent with experiment given the instrumental resolution. As discussed later, however, this direct pathway cannot explain the trends in the angular data and requires the simultaneous absorption of more photons

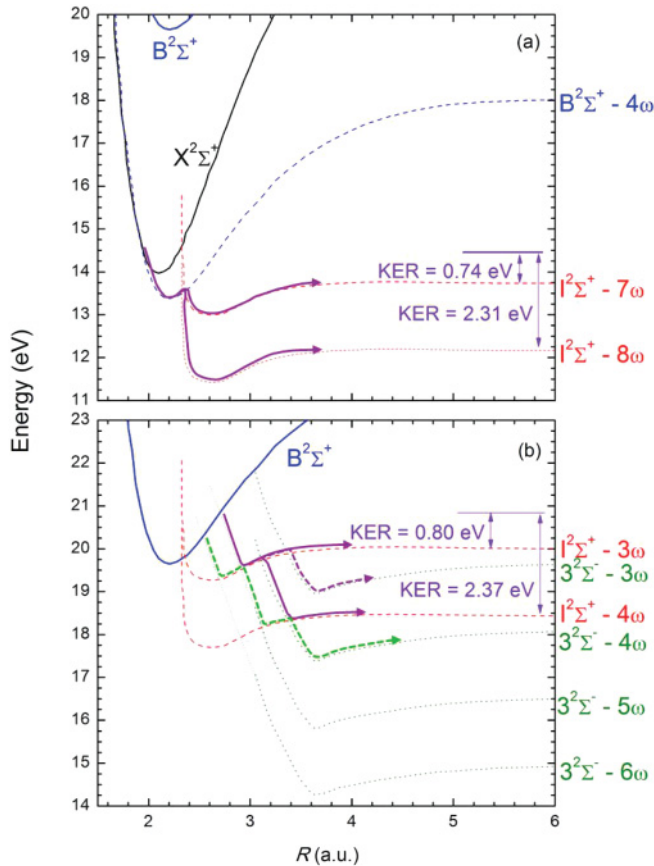


FIG. 6. (Color online) Field-dressed potential-energy curves of CO^+ and suggested pathways leading to the observed KER distributions of O^+ fragments for peaks α and β in the inset of Fig. 5. (a) The $X^2\Sigma^+ \rightarrow B^2\Sigma^+ - 4\omega \rightarrow I^2\Sigma^+ - n\omega$ pathways, with the pathways indicated by the violet arrows. (b) The $B^2\Sigma^+ \rightarrow 3^2\Sigma^- - 5\omega \rightarrow I^2\Sigma^+ - 3\omega$ and the $B^2\Sigma^+ \rightarrow 3^2\Sigma^- - 5\omega \rightarrow I^2\Sigma^+ - 3\omega \rightarrow 3^2\Sigma^- - 3\omega$, with a $\text{C}^+ + \text{O}$ final state and an expected KER of 1.2 eV. The dashed green arrow represents a $B^2\Sigma^+ \rightarrow 3^2\Sigma^- - 6\omega \rightarrow I^2\Sigma^+ - 3\omega \rightarrow 3^2\Sigma^- - 5\omega \rightarrow I^2\Sigma^+ - 4\omega \rightarrow 3^2\Sigma^- - 4\omega$ path with an expected KER of 2.3 eV.

than an alternative route. Direct pathways starting with excited electronic states do not produce KER distributions that match our results either, although we note that direct transitions to the $I^2\Sigma^+ - n\omega$ state from the $A^2\Pi$ ($n = 5$), $C^2\Delta$ ($n = 2$), $3^2\Sigma^+$ ($n = 1$), and $2^2\Sigma^-$ ($n = 1$) states all result in KER distributions peaked near zero and could explain the KER distribution for the FTL pulses shown in Figs. 4 and 5.

Having failed to find a satisfactory set of direct pathways for the optimal pulse data, it seems likely that the optimal pulse populates the $\text{C} + \text{O}^+$ final state via an indirect process that involves at least one intermediate state along the path. This conclusion is also supported by the structure of the optimal pulse (see Fig. 2) which has the potential to allow the wavepacket evolution to extend far from equilibrium, allowing time for a bound nuclear wave packet to bounce multiple times between turning points prior to a final excitation. Considering the relatively poor overlap between the initial CO wave

function and the $I^2\Sigma^+$ state of CO^+ , this complex pulse structure could be an advantage when seeking to selectively dissociate to $\text{C} + \text{O}^+$ rather than $\text{C}^+ + \text{O}$.

Two sets of possible indirect pathways are illustrated in Fig. 6. The first of these pathways, shown in Fig. 6(a), proceeds from the $\text{CO}^+ X^2\Sigma^+$ ground state through the $B^2\Sigma^+ - 4\omega$ intermediate state and ultimately results in a KER distribution peaked at 0.74 eV. An additional photon results in a KER peak of 2.31 eV. These results are reasonably consistent with our data. Since the optimal laser pulse has a complex structure spread over several hundred femtoseconds, compared to ~ 45 fs for the FTL pulse, it would seem that high intensity is not an essential ingredient of the optimal pulse. This particular indirect path requires only the sequential absorption of four followed by three (or four) photons for dissociation rather than the simultaneous absorption of seven or eight photons needed for the direct route to the $I^2\Sigma^+ - n\omega$ state.

An alternative set of indirect pathways, illustrated in Fig. 6(b) by the solid violet arrows, begins with the $B^2\Sigma^+$ state (populated directly from CO) and also fits the KER data reasonably well. There are, however, two difficulties with this set of potential paths. First, as denoted by the dashed violet arrow, there should be an intermediate pathway which would lead to a $\text{C}^+(^2P) + \text{O}(^3P)$ final state and an expected KER of 1.2 eV. The data presented in Fig. 7 suggests that this is not a primary pathway, although there is some KER yield in this region. Likewise, another pathway leading to $\text{C}^+(^2P) + \text{O}(^3P)$, marked by the dashed green arrow in Fig. 6(b), should also exist and have an expected KER of 2.3 eV, a value that falls between the observed peaks at ~ 2.1 and ~ 2.7 eV in Fig. 7. Second, it would require four additional photons to populate the $B^2\Sigma^+$ state (from CO) compared to the ground $X^2\Sigma^+$ state. As a result of these factors, the pathways identified in Fig. 6(a) provide the most plausible match to our results.

As seen in Figs. 4 and 8, VMI also provides angular information. We note that the most likely $\text{C} + \text{O}^+$ pathways all involve parallel transitions ($^2\Sigma^+ \rightarrow I^2\Sigma^+$), with no change in the angular momentum quantum number ($\Delta\Lambda = 0$). The angular distributions for peaks α and β in Fig. 5 are shown

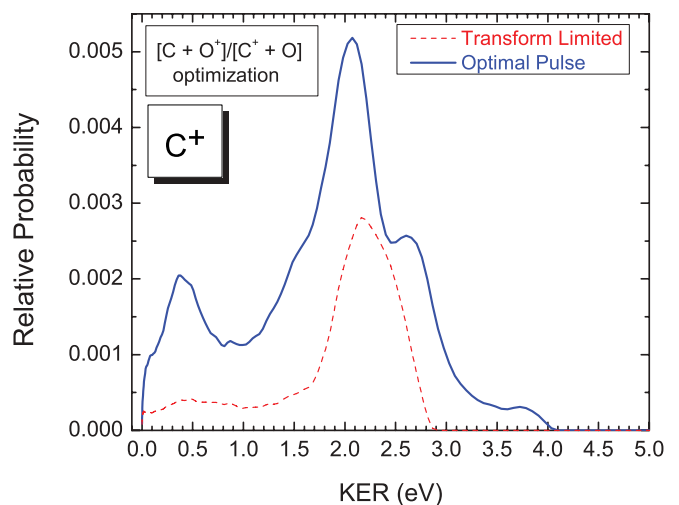


FIG. 7. (Color online) Relative probability vs KER for $\text{C}^+ + \text{O}$ dissociative ionization produced by FTL pulses (dashed red line) and pulses that optimize $[\text{C} + \text{O}^+]/[\text{C}^+ + \text{O}]$ (solid blue line).

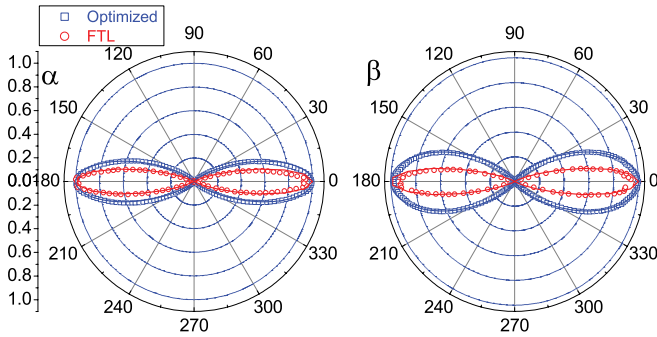


FIG. 8. (Color online) Polar plots of the normalized angular distributions obtained for the $C + O^+$ channel with laser pulses tailored to optimize $[C + O^+]/[C^+ + O]$ feedback targets (blue) and with FTL pulses (red). The left distribution is for peak α (0.53–1.48 eV) from the inset of Fig. 5, and the right distribution is for peak β (1.86–2.60 eV). The laser polarization is along the 0° - 180° axis. Both FTL distributions are fit with a $\cos^{32}(\theta)$ (red lines) function. The optimized data are fit with $\cos^{12}(\theta)$ and $\cos^6(\theta)$ (blue lines) for the left and right distributions, respectively.

in Fig. 8. The optimal pulse produces angular distributions that are best fit with $\cos^{12}(\theta)$ for peak α and $\cos^6(\theta)$ for peak β . In contrast, the FTL pulses produce a much higher degree of alignment, fitting a $\cos^{32}(\theta)$ distribution for both peaks. This result highlights the difference between the FTL and the optimized pulses and indicates that a full understanding of the resulting angular distributions will most likely require more detailed theoretical work. One can speculate, however, that the relatively short and intense FTL pulses are driving population to some of the many direct dissociation channels that result in strongly aligned $C + O^+$ fragments with near-zero KER, which can be seen in Fig. 5. The more complex optimized pulse, on the other hand, produces fragments with less rigid alignment. The angular information also supports the indirect $X^2\Sigma^+ \rightarrow B^2\Sigma^+ - 4\omega \rightarrow I^2\Sigma^+ - n\omega$ pathways rather than the direct $X^2\Sigma^+ \rightarrow I^2\Sigma^+ - n\omega$ ($n = 7$ and 8) pathways because the latter route requires the simultaneous absorption of three or four additional photons and thus should be more strongly aligned with the polarization axis.

More importantly, the angular data is key for understanding another aspect of the control achieved in the previous experiment [17]. The high-resolution time-of-flight (TOF) spectrometer used in that experiment had only a small opening along the TOF axis, limiting the solid angle to 2.2×10^{-4} sr along the 0° - 180° axis. With the laser pulses linearly polarized along the TOF axis, fragments with momentum away from the polarization direction are discriminated. This is not the case with the VMI spectrometer.

Laser pulses that optimized $[C + O^+]/[C^+ + O]$ in the TOF experiment [17] took advantage of this feature to suppress the C^+ yield. Figure 4 shows a higher yield of low-energy (KER ≤ 3 eV) C^+ fragments away from the polarization direction compared to the FTL pulse. The effect, while apparent, is not nearly as pronounced with the O^+ fragments.

Coupling this information with the earlier pathway analysis allows us to reach a tenable conclusion about the control mechanism. Due to its complex nature and extended duration [17], the optimal pulse shape is able to accomplish two

simultaneous outcomes. First, it drives the $CO^+ \rightarrow C + O^+$ dissociation through the indirect pathways shown in Fig. 6(a) and away from the many direct pathways which result in zero KER. The resulting O^+ fragments, while not as strongly aligned as observed with the FTL pulse, are nonetheless parallel transitions. Populating the routes in Fig. 6(a) has the corresponding effect of concurrently opening a nearby indirect pathway leading to C^+ fragments, namely, $X^2\Sigma^+ \rightarrow B^2\Sigma^+ - 4\omega \rightarrow D^2\Pi - 6\omega$. This pathway has both an expected KER of 2.1 eV, which overlaps the prominent peak in Fig. 7, and $\Delta\Lambda = 1$, thus producing the C^+ fragments at large angles from the laser polarization. These fragments were less likely to exit the TOF spectrometer than the O^+ fragments, resulting in suppression of C^+ yield and the observed control.

When the objective was the optimization of $[C^+ + O]/[C + O^+]$, the optimal pulse produces both O^+ and C^+ fragments predominately along the polarization axis (see Fig. 4). In this case, however, many of the states that dissociate into $C^+ + O$ may be accessed with lower intensity than the $C + O^+$ final states, and so more C^+ yield is expected. These two conditions, however, are satisfied in large part by the FTL pulse as well, and so it is difficult to identify a pulse that does significantly better than the FTL pulse. Indeed, the optimal pulse in these cases closely resembles a FTL pulse [17].

B. Two-dimensional VMI as feedback

In addition to using VMI to help discern the mechanisms underlying the control of the dissociative ionization of CO, we have used the raw 2D images directly in the adaptive control loop. Our initial idea was to use the same feedback targets as employed in the TOF experiment [17]. While partially successful, in retrospect it is clear how these attempts could be improved. Given the interest in incorporating VMI into closed-loop control [32,38,39], it is worthwhile to briefly review our results and suggest several ways to improve this technique in the future.

The use of images in adaptive femtosecond control is not unprecedented. Molecular orientation and alignment experiments (e.g., Ref. [38]) are one class of experiments in which the raw VMI data may give a reliable feedback signal. In another example, Chen and co-workers [32] examined the Coulomb explosion of CO_2^{6+} . In those experiments, each image corresponded to a single laser shot and correlation techniques were used to identify the $O^{2+} + C^{2+} + O^{2+}$ events of interest. In our approach, in which we examine the dissociative single-ionization channels, the identification of a low-energy C^+ or O^+ ion is sufficient, and we do not need to use statistical correlation methods such as image labeling or selective averaging.

We do, however, need to choose a robust fitness target from a portion of the image. Because the raw image is a 2D projection of a 3D momentum distribution, there is some ambiguity in this process because of the integration along the spectrometer axis. Several of our attempts are illustrated in Fig. 9.

Since we are interested in the dissociative single-ionization channel, the most logical place to start would be to select fragments with momentum below the threshold for double ionization. A circular gate, as shown in Fig. 9(a), allows

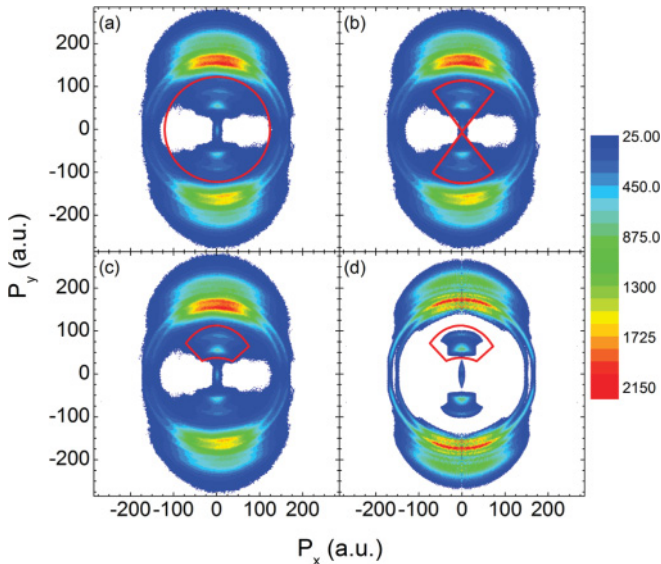


FIG. 9. (Color online) (a)–(c) Raw, unsymmetrized, 2D VMI plots of O^+ fragments with various feedback gate settings as used in the experiment and discussed in the text. The interior part of the plot, defined by the red circle in plot (a), contains the dissociation channels, while the outside contains higher-energy fragments from multiple ionization of CO. (d) Inverted image representing a slice at $p_z = 0$ of the 3D momentum distribution of the same image after being symmetrized and inverted to remove the undesirable azimuthal contribution. The feedback gates derived from the raw VMI plots contain more noise, and therefore a gate on an inverted image is desirable.

the user to select just this sort of situation and seemingly exclude most of the double ionization, which dominates on the outer part of the image. Our first attempts used this sort of feedback gate on both the C^+ and O^+ fragments, with the fitness defined as the ratio of these two integrated signals. Under these conditions, the genetic algorithm (GA) was often unable to converge on a solution. We suspect that the primary reason for this result is the contribution from higher velocity fragments that are ejected from the interaction region at angles that allow them to land in the circular feedback gate. A comparison between Figs. 9(a) and 9(d) shows that most of the dissociative single-ionization signal is localized in a small region and that the gate contains a large region that primarily contains noise.

The effect of this noisy region can be minimized using the feedback gate shown in Fig. 9(b). A primary difficulty with this configuration, however, is that if there is significant yield in the very center of the image (i.e., at zero transverse momentum), the placement of the crossover point becomes critical, and the experiment becomes very sensitive to small fluctuations of the laser focus location. In addition, if there is a molecular ion that arrives in the center of the detector prior to the fragments of interest, these ions can trigger some signal on the phosphor even with low voltage on the microchannel plates. In the case of a carbon monoxide, this role is played by CO^{2+} arriving in a few channels near the center of the detector. As a result of these two issues, we found that the “bow-tie” arrangement shown in Fig. 9(b) was somewhat unstable as a gate on a 2D image.

The best gate configuration we identified is shown in Fig. 9(c). As is the case in Fig. 9(b), this setting maximizes the signal-to-noise ratio but without having to deal with the potentially troublesome center of the image. After experimenting with these settings, we observe that many GA-determined trial pulses tend to produce the same basic features in the image, but the radius of the feature location often varies from pulse to pulse. Thus, when seeking to separate a channel for feedback purposes, radial isolation from neighboring channels is desirable. In this respect, the inverted image in Fig. 9(d) is clearly superior. To use a $p_z = 0$ slice through the 3D momentum distribution for feedback, however, requires the development of an inversion technique that is both rapid and sufficiently accurate.

Nevertheless, we were able to obtain some enhancement in the $[C^+ + O]/[C + O^+]$ or $[C + O^+]/[C^+ + O]$ ratios using the settings shown in Fig. 9(c), although we observed less gain than we obtained with our previous TOF-based feedback scheme [17]. The resulting optimal pulses did not even qualitatively resemble the optimal pulses from the earlier experiment. In hindsight this result is not surprising, considering how much the previous control relied on angular discrimination that is avoided in the current VMI measurements. Despite this limitation, the enhancement accomplished with the 2D VMI feedback illustrates control of the dissociative ionization process.

This work demonstrates that 2D images obtained from the well-established VMI technique can be used as a rapid source of feedback in adaptive femtosecond control. On the other hand, there are limitations to using the raw images as a feedback source. Inversion of these images to recover the 3D information is traditionally a process that is done after the data has been gathered. While a number of inversion techniques exist [34], many of them require some prior knowledge of the image characteristics or take too long to be used in the adaptive control loop. In recent years, however, there have been some promising examples of rapid inversion techniques [56]. We are currently investigating the possibility of inverting the images online prior to deriving a fitness value from the image. Working with the full 3D momentum representation should lead to more robust image-based feedback.

IV. SUMMARY

We have demonstrated the utility of VMI for *a posteriori* determination of the mechanisms underlying the ability of shaped ultrafast laser pulses to manipulate the fragmentation branching ratio of CO^+ . Even lacking knowledge of some of the relevant potential-energy curves for highly excited states of CO^+ , VMI revealed information about the control process that could not be recovered from time-of-flight results [17]. In particular, we show that some of our previous control was due to an angular discrimination effect and identify dissociation pathways that used this experimental feature to enhance the $[C + O^+]/[C^+ + O]$ ratio. The identified pathways are consistent with the observed KER distributions and can be reconciled with the major features of the optimized laser pulses.

Moreover, in the second part of this work, we have demonstrated that 2D images obtained with the VMI method

may be included in a rapidly running adaptive control loop. In principle, this advancement enables the experimenter to select a very specific target for enhancement using adaptive femtosecond control techniques. Coupling this ability with different pulse parametrization schemes could lead to further understanding of adaptive femtosecond control. In order to achieve this goal, however, it will most likely be necessary to avoid some of the difficulties of working with the two-dimensional projection of the three-dimensional momentum distribution. Based upon our initial progress, we are optimistic that real time image inversion can be developed for this purpose.

ACKNOWLEDGMENTS

The authors acknowledge Professor Zenghu Chang and his group members for providing laser expertise and thank Drew Doshier for help with the data acquisition. This work was supported by the National Science Foundation and by the Chemical Sciences, Geosciences, and Biosciences Division, Office of Basic Energy Sciences, Office of Science, US Department of Energy. E.W. acknowledges additional support from the Augustana College Research and Artist Fund. B.B. and M.F.K. are grateful for support by the DFG via the Emmy-Noether and International Collaboration in Chemistry programs.

-
- [1] A. Assion, T. Baumert, M. Bergt, T. Brixner, B. Kiefer, V. Seyfried, M. Strehle, and G. Gerber, *Science* **282**, 919 (1998).
- [2] R. J. Levis, G. M. Menkir, and H. Rabitz, *Science* **292**, 709 (2001).
- [3] M. Bergt, T. Brixner, B. Kiefer, M. Strehle, and G. Gerber, *J. Phys. Chem. A* **103**, 10381 (1999).
- [4] C. Daniel, J. Full, L. González, C. Lupulescu, J. Manz, A. Merli, Š. Vajda, and L. Wöste, *Science* **299**, 536 (2003).
- [5] E. Wells, K. J. Betsch, C. W. S. Conover, Merrick J. DeWitt, D. Pinkham, and R. R. Jones, *Phys. Rev. A* **72**, 063406 (2005).
- [6] T. Laarmann, I. Shchatsinin, A. Stalmashonak, M. Boyle, N. Zhavoronkov, J. Handt, R. Schmidt, C. P. Schulz, and I. V. Hertel, *Phys. Rev. Lett.* **98**, 058302 (2007).
- [7] M. Kotur, T. Weinacht, B. J. Pearson, and S. Matsika, *J. Chem. Phys.* **130**, 134311 (2009).
- [8] T. Brixner, B. Kiefer, and G. Gerber, *Chem. Phys.* **267**, 241 (2001).
- [9] M. Bergt, T. Brixner, C. Dietl, B. Kiefer, and G. Gerber, *J. Organomet. Chem.* **661**, 199 (2002).
- [10] T. Brixner, N. H. Damrauer, G. Krampert, P. Niklaus, and G. Gerber, *J. Mod. Opt.* **50**, 539 (2003).
- [11] R. J. Levis and H. A. Rabitz, *J. Phys. Chem. A* **106**, 6427 (2002).
- [12] C. Daniel *et al.*, *Chem. Phys.* **267**, 247 (2001).
- [13] D. Cardoza, F. Langhojer, C. Trallero-Herrero, O. L. A. Monti, and T. Weinacht, *Phys. Rev. A* **70**, 053406 (2004).
- [14] F. Langhojer, D. Cardoza, M. Baertschy, and T. Weinacht, *J. Chem. Phys.* **122**, 014102 (2005).
- [15] D. Cardoza, M. Baertschy, and T. Weinacht, *Chem. Phys. Lett.* **411**, 311 (2005).
- [16] D. Cardoza, B. J. Pearson, M. Baertschy, and T. Weinacht, *Photochem. Photobiol. A* **180**, 277 (2006).
- [17] E. Wells *et al.*, *Phys. Rev. A* **80**, 063402 (2009).
- [18] E. Wells, J. McKenna, A. M. Sayler, B. Jochim, N. Gregerson, R. Averin, M. Zohrabi, K. D. Carnes, and I. Ben Itzhak, *J. Phys. B* **43**, 015101 (2010).
- [19] A. Monmayrant, S. Weber, and B. Chatal, *J. Phys. B* **43**, 103001 (2010).
- [20] R. S. Judson and H. Rabitz, *Phys. Rev. Lett.* **68**, 1500 (1992).
- [21] B. J. Pearson, J. L. White, T. C. Weinacht, and P. H. Bucksbaum, *Phys. Rev. A* **63**, 063412 (2001).
- [22] D. Zeidler, S. Frey, K.-L. Kompa, and M. Motzkus, *Phys. Rev. A* **64**, 023420 (2001).
- [23] J. H. Posthumus, *Rep. Prog. Phys.* **67**, 623 (2004).
- [24] V. V. Lozovoy, X. Zhu, T. C. Gunaratne, D. A. Harris, J. C. Shane, and M. Dantus, *J. Phys. Chem. A* **112**, 3789 (2008).
- [25] F. Krausz and M. Ivanov, *Rev. Mod. Phys.* **81**, 163 (2009).
- [26] K. Ohmori, *Annu. Rev. Phys. Chem.* **60**, 487 (2009).
- [27] H. Rabitz, M. Hsieh, and C. Rosenthal, *Science* **303**, 998 (2004).
- [28] R. Chakrabarti and H. Rabitz, *Int. Rev. Phys. Chem.* **26**, 671 (2007).
- [29] D. Cardoza, M. Baertschy, and T. Weinacht, *J. Chem. Phys.* **123**, 074315 (2005).
- [30] R. A. Bartels, M. M. Murnane, H. C. Kapteyn, I. Christov, and H. Rabitz, *Phys. Rev. A* **70**, 043404 (2004).
- [31] C. Trallero, B. J. Pearson, T. Weinacht, K. Gilliard, and S. Matsika, *J. Chem. Phys.* **128**, 123107 (2008).
- [32] G.-Y. Chen, Z. W. Wang, and W. T. Hill III, *Phys. Rev. A* **79**, 011401(R) (2009).
- [33] J. Roslund and H. Rabitz, *Phys. Rev. A* **80**, 013408 (2009).
- [34] B. J. Whitaker, *Imaging in Molecular Dynamics: Technology and Applications (A User's Guide)* (Cambridge University Press, Cambridge, 2003).
- [35] A. T. J. B. Eppink and D. H. Parker, *Rev. Sci. Instrum.* **68**, 3477 (1997).
- [36] D. Irimia and M. H. M. Janssen, *J. Chem. Phys.* **132**, 234302 (2010).
- [37] J. Ullrich, R. Moshhammer, A. Dorn, R. Dörner, L. Ph. H. Schmidt, and H. Schmidt-Böcking, *Rep. Prog. Phys.* **66**, 1463 (2003).
- [38] O. Ghafur, A. Rouzee, A. Gijssbertsen, W. K. Siu, S. Stolte, and M. J. J. Vrakking, *Nature Phys.* **5**, 289 (2009).
- [39] M. Krug, T. Bayer, M. Wollenhaupt, C. Sarpe-Tudoran, T. Baumert, S. S. Ivonov, and N. V. Vitanov, *New. J. Phys.* **11**, 105051 (2009).
- [40] F. Verluise, V. Laude, Z. Cheng, Ch. Spielmann, and P. Tournois, *Opt. Lett.* **25**, 575 (2000).
- [41] S. De *et al.*, *Phys. Rev. Lett.* **103**, 153002 (2009).
- [42] D. Ray *et al.*, *Phys. Rev. Lett.* **103**, 223201 (2009).
- [43] R. Trebino, *Frequency-Resolved Optical Gating: The Measurement of Ultrashort Laser Pulses* (Kluwer Academic, Norwell, MA, 2002).
- [44] C. Bordas, F. Paulig, H. Helm, and D. L. Huestis, *Rev. Sci. Instrum.* **67**, 2257 (1996).

- [45] M. J. J. Vrakking, *Rev. Sci. Instrum.* **72**, 4084 (2001).
- [46] G. A. Garcia, L. Nahon, and I. Powis, *Rev. Sci. Instrum.* **75**, 4989 (2004).
- [47] I. T. Jolliffe, *Principal Component Analysis*, 2nd ed. (Springer, Berlin, 2002).
- [48] K. Okada and S. Iwata, *J. Chem. Phys.* **112**, 1804 (2000).
- [49] M. Carlsson-Göthe, B. Wannberg, F. Falk, L. Karlsson, S. Svensson, and P. Baltzer, *Phys. Rev. A* **44**, R17 (1991).
- [50] M. Lundqvist, P. Baltzer, D. Edvardsson, L. Karlsson, and B. Wannberg, *Phys. Rev. Lett.* **75**, 1058 (1995).
- [51] A. S. Alnaser *et al.*, *Phys. Rev. Lett.* **93**, 183202 (2004).
- [52] I. Znakovskaya, P. von den Hoff, S. Zherebtsov, A. Wirth, O. Herrwerth, M. J. J. Vrakking, R. de Vivie-Riedle, and M. F. Kling, *Phys. Rev. Lett.* **103**, 103002 (2009).
- [53] A. Hishikawa, S. Liu, A. Iwasaki, and K. Yammanouchi, *J. Chem. Phys.* **114**, 9856 (2001).
- [54] A. M. Saylor, P. Q. Wang, K. D. Carnes, B. D. Esry, and I. Ben Itzhak, *Phys. Rev. A* **75**, 063420 (2007).
- [55] B. Gaire, J. McKenna, A. M. Saylor, Nora G. Johnson, E. Parke, K. D. Carnes, B. D. Esry, and I. Ben Itzhak, *Phys. Rev. A* **78**, 033430 (2008).
- [56] G. Roberts, J. Nixon, J. Lecointre, E. Wrede, and J. Verlet, *Rev. Sci. Instrum.* **80**, 053104 (2009).